SpaceOps-2023, ID #161
17th International Conference on Space Operations, Dubai, United Arab Emirates, 6 - 10 March 2023.

Comparison of Spacecraft Vision-Based Navigation Methods and Proposal of a Novel Shadow-Correction Block

Aurélia Bourgeaux[a]∗, Ramón María García Alarcia[b]

[a] *Orbit Determination Section, Centre National d'Études Spatiales (CNES), 18 avenue Édouard Belin, 31401 TOULOUSE CEDEX 9, France*, aurelia.bourgeaux@cnes.fr

[b] *Department of Aerospace and Geodesy, Technical University of Munich (TUM), Caroline-Herschel-Straße 100/II, 85521 Ottobrunn, Germany*, ramon.garcia-alarcia@tum.de
This work was performed by the coauthor during an internship at CNES.

∗ Corresponding Author

Abstract

Since humankind began sending spacecraft to explore our Solar System around 60 years ago, navigation, and operations in general, around and on the explored bodies have evolved substantially. Knowledge on the physics and the environment, and advances in hardware and software systems have been cornerstone to allowing advanced concepts for the execution of interplanetary missions. Indeed, during the last years, new techniques for navigation in such missions have emerged. Among them, Vision-Based Navigation (VBN) has stood out as one of the most promising techniques for navigation around small bodies. This technique leverages on taking images with an on-board camera in the satellite, with the goal of extracting useful information for the relative positioning of the satellite with respect to the navigated body. In general terms, a treatment of the image given by the camera is performed to extract information. Then, this information is transformed into data that can be used by an algorithm of orbit determination, giving the satellite's state (position and velocity) as a function of time. There are different families of VBN algorithms, some with current in-flight experience (e.g. centroid determination via centre of brightness) and some being proposed in the literature as an enhancement. In this work, VBN algorithms from the family of centroid determination via ellipse fitting, which promises an increase of accuracy over current techniques (at the cost of higher required computational power) have been coded on MATLAB, generating data that is compatible with CNES' orbit determination tools. The different alternative implementations have been tested and benchmarked with synthetic images of asteroids generated by an internal CNES tool. This work confirms the higher accuracy of this family of algorithms with respect to current centre of brightness methods. It also selects the best algorithmic combination for different scenarios. Additionally, it proposes a novel correction method that diminishes the disturbing effect of

large areas of shadow on the navigated body.

Keywords: Vision-Based Navigation, Line-Of-Sight vector, centroid determination, ellipse fitting, small bodies, shadowing correction

Acronyms/Abbreviations
Centre Of Brightness (COB)
Connected Component Analysis (CCA)
Centre National d'Études Spatiales (CNES)
Deep Learning (DL)
Field Of View (FOV)
Graphical User Interface (GUI)
Infrared (IR)
Line-Of-Sight (LOS)
M-Estimator Sample Consensus (MSAC)
Random Sample Consensus (RANSAC)
Visible (VIS)
Vision Based Navigation (VBN)

1. Introduction

Vision-Based Navigation (VBN) is a technique that uses images taken by a spacecraft's camera to calculate its relative position and attitude, particularly useful for close operations around small and irregular bodies like asteroids and comets. VBN overcomes the limitations of using Earth-based antennas, such as loss of real-time reactivity due to signal delays. It involves a number of different techniques, with the simplest and less accurate methods being the estimation of the navigated body's centroid as the image's center of brightness, which has already been proven in flight. With advancements in space hardware, more complex and accurate techniques will become possible, leading to increased autonomy, speed, and safety in space navigation.

In this study, various VBN algorithms that estimate the body's centroid by fitting an ellipse (not yet tested in flight, but showing promise for more accurate results) have been analyzed, selected and implemented in MATLAB. A VBN Simulator was developed that can take asteroid images as input and output navigation data that is compatible with CNES' navigation tools. Simulations were run for nominal, degraded, corrected and real scenarios. During testing, it was observed that the ellipse fitting algorithms lose reliability in certain lighting conditions where irregular asteroids present large shadowed areas on their surface. A novel contribution of this work is the development of a shadow correction block using different strategies, which significantly improves accuracy. Results confirm the higher accuracy of centroid determination via ellipse fitting and suggest its use in degraded image data and when computation time is not a constraint. The best algorithm combinations were determined and insights on when to use each were gained.

2. Material and methods

This work has developed a VBN simulator that tests different selected VBN algorithms and compares their results. Built in MATLAB, it accepts asteroid images and their corresponding references for computing the ground truth of each image, and outputs the estimated centroid in pixel coordinates, the Line-Of-Sight vector from the spacecraft to it, the simulation error committed with respect to the reference and the algorithm simulation time. These values enable the comparison of different VBN algorithms to select the best combination.

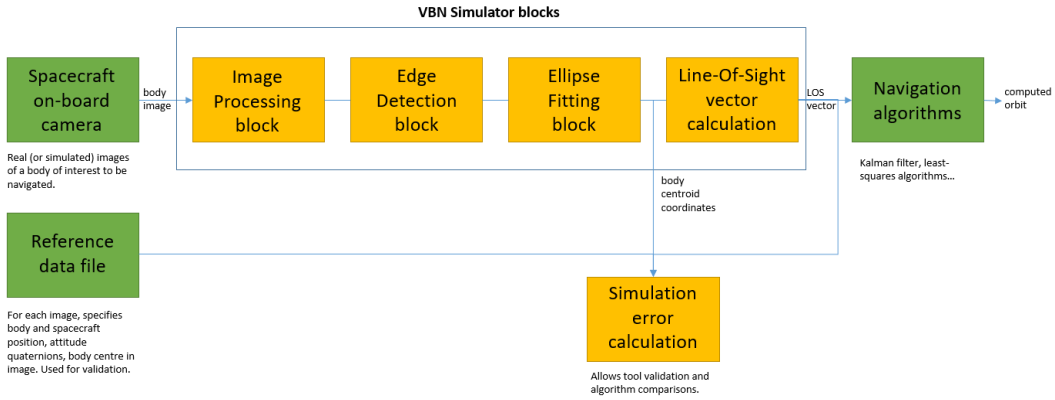

Figure 1: Block diagram of the VBN simulator, depicting inputs, calculation blocks, and outputs.

The VBN simulator was designed in a modular fashion, utilising classes and reading configuration data from XML files for easy modifications. A Graphical User Interface (GUI) was also developed to facilitate the creation of simulations, with the goal of remaining an accessible tool for CNES to test different VBN strategies. The simulator was divided into different blocks, corresponding to the initial stages of a typical VBN chain: Image Processing, Edge Detection, Ellipse Fitting, LOS computation.

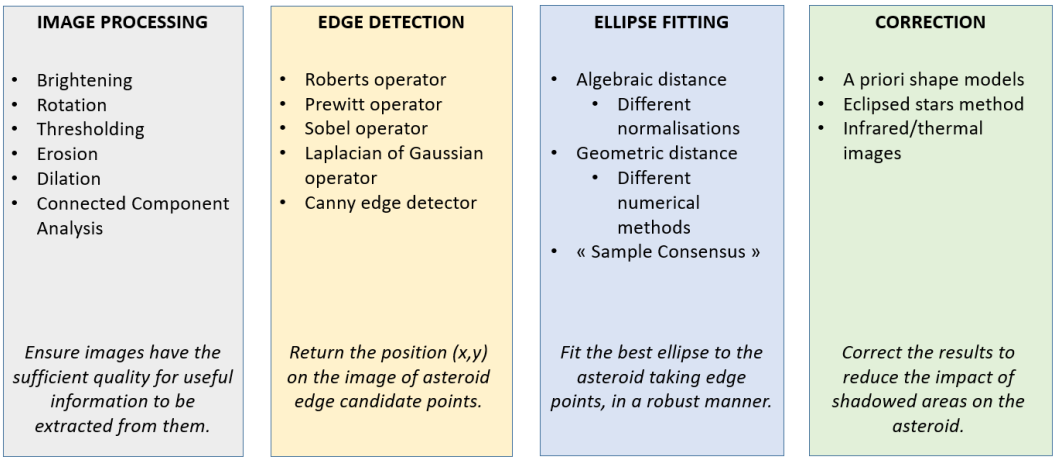

Figure 2: Modular blocks of the VBN simulator, with implemented techniques and description.

The Image Processing block of the simulator implemented algorithms for brightening, rotation of the image, thresholding, erosion, dilation, and Connected Component Analysis to prepare the image

for information extraction [Samet and Tamminen, 1988]. In the Edge Detection block, the Roberts operator [Roberts, 1965], the Prewitt operator [Prewitt, 1970], the Sobel [Sobel and Feldman, 1973] operator, the Laplacian of Gaussian operator [Kong et al., 2013], and the Canny edge detector [Canny, 1986] were used to determine the contour of the navigated body.

In the Ellipse Fitting block, the direct fitting via a least-squares problem resolution with the $A+C=1$ normalisation, the $F=1$ normalisation, the $4AC-B^2=1$ constraint, and an improved resolution [Christian and Lightsey, 2010], were included. In addition, the numerical resolution of the least-squares problem using geometric distance, with the Gauss-Newton [Ahn et al., 1999] and the Levenberg-Marquadt algorithms [Barham and Drane, 1972], were included. Finally, robust sample consensus methods, in particular the Random Sample Consensus [Fischler and Bolles, 1981] (RANSAC) and the M-Estimator Sample Consensus (MSAC) [Torr and Zisserman, 2000], were added as well. The goal of these algorithms is to fit an ellipse to a succession of locations previously considered to determine the edge of the navigated body. The fitted ellipse provides instant access to the body centroid in the pixel coordinate frame. Then, from the centroid, a LOS vector can be quickly computed in the camera frame.

During simulations, it was found that shadowed areas on the asteroid can greatly reduce VBN chain performance. These shadowed areas are the result of the inherent irregularity of asteroids and particular solar light angles of incidence. To mitigate this, an optional correction block was added to the simulator. This block incorporates new data into the chain and re-runs the ellipse fitting block. The type of data that it can integrate is the following:

- ***A priori* shape model**: uses information on the semi-major and semi-minor axes of the asteroid and distance to it to generate a 2D ellipse to match to the asteroid on the image. A future work is to read 3D shape model files defined by harmonic sphere parameters or by finite elements. The functioning of this correction method is depicted by Figure 3: a 2D ellipse is generated from input data, and then is translated and rotated along the image until it fits the body of interest, searching to maximise a cross-correlation function.

- **Eclipsed stars position information**: knowing the attitude of the spacecraft, a "window" of sky can be generated. This window displays the stars that would be visible to the spacecraft's camera if it were pointing in a specific direction, ignoring the presence of the asteroid. Stars that are shaded by the asteroid can be identified by combining the image including the asteroid and the equivalent window of sky. Then, by taking these shadowed stars as new, additional edge candidate points, and applying a convex hull algorithm to keep only the most outermost points. Figure 4a depicts the functioning of this method.

- **Infrared/thermal equivalent images**: in infrared (IR) images, shadows do not appear and the whole structure of the asteroid is visible [Okada, 2020], as depicted per Figure 4b. IR images can be used to correct the result obtained with visible (VIS) images (by computing a weighted mean or a via more complex hybridisation involving Kalman filters, for instance), or can be used directly as the simulation input. However, IR cameras are not so common in interplanetary missions, and their resolution and Field Of View (FOV) is significantly lower than VIS spectrum cameras.

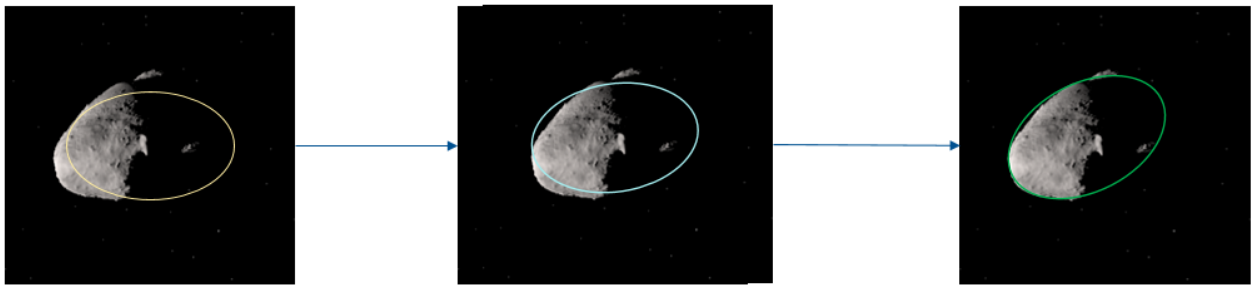

Figure 3: The *a priori* shape model data is used to generate an ellipse according to input data. The ellipse is then iteratively displaced and rotated until it fits the body of interest by maximising a cross-correlation function.

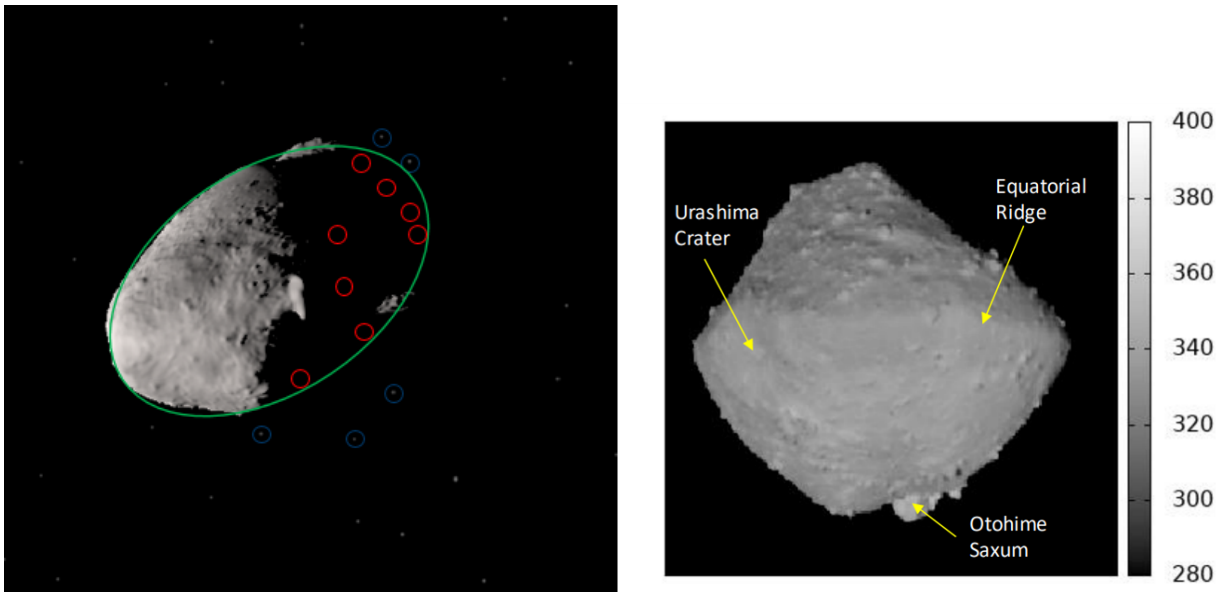

(a) Ecipsed stars correction method (b) Infrared images correction method [Okada, 2020]

Figure 4: (a) Usage of eclipsed star positions in order to enlarge the initially fitted ellipse. Blue circles encircle (some) stars that are visible on the image. Red circles encircle stars that are hidden by the asteroid but on a shadowed area, and that should be visible if there was not an asteroid in front. The green ellipse shows the result of applying a convex hull algorithm enlarging the original fitted ellipse with the use of eclipsed stars. / (b) Real infrared image taken by Hayabusa 2's Thermal Infrared Imager (TIR) camera of asteroid's Ryugu, demonstrating the feasibility of using these images for VBN since all the body is clearly seen without shadows (extracted from [Okada, 2020]).

3. Theory and calculation

The goal of a VBN system is to retrieve available navigation observables from raw images captured by a spacecraft [Li et al., 2013], and then use them with a navigation filter in order to determine the

orbit of the spacecraft. This section explains the theory behind centroid determination via ellipse fitting, including the algorithms used for image processing, edge detection, ellipse fitting, and the computation of the LOS vector, as well as the camera model and reference frame used. It also introduces the simulations performed to compare different algorithmic combinations of centroid determination via ellipse fitting and the input parameters of the simulations.

3.1 Reference frames

The International Celestial Reference Frame (ICRF) is used to describe the position and attitude of the spacecraft in the reference files associated with input images, in order to calculate the ground truth LOS vector. The image frame is used to express the centroid coordinates, with the origin at the top left corner of the image, the x-axis increasing to the right, and the y-axis increasing downward. The camera frame is used to express the LOS vector, with the origin at the center of the image, the z-axis pointing outward, the x-axis increasing to the right, and the y-axis increasing upward. All dates and times are in the Barycentric Dynamical Time (TDB) scale.

3.2 Camera model

The simulator uses a pinhole camera model, in which each point on the target emits a single ray, which maps to a point on the focal frame [Li et al., 2013]. In this model, a point $P(X, Y, Z)$ on the navigated body maps to pixel coordinates $[u, v]$ as shown in Equation 1. If the pixel coordinates $[u, v]$ of a point i on the navigated body are known, the LOS vector e from the spacecraft to point i in the camera frame C can be calculated using Equation 2.

$$u = \frac{X}{Z} f \qquad v = \frac{Y}{Z} f \tag{1}$$

$$e_i^C = \frac{1}{\sqrt{u_i^2 + v_i^2 + f^2}} \begin{bmatrix} u_i \\ v_i \\ f \end{bmatrix} \tag{2}$$

3.3 Image Processing algorithms

The Image Processing block aims to improve the input image quality for proper contour determination. Techniques used include image brightening, rotation to force the entrance of the sunlight from the left side of the image (which is said to be beneficial for the ensuing Ellipse Fitting [Christian and Lightsey, 2010]), thresholding, erosion, dilation, and Connected Component Analysis (CCA). Erosion, which involves reducing boundaries of foreground pixels using a structuring element, is used to remove external features in the image for ellipse fitting. Mathematically, erosion (defined in Equation 3) is represented by the $\ominus$ symbol and is defined as $A, \ominus, B$, where B_z is the translation of B by vector z and evaluated as a subset of A.

$$A \ominus B = \{z \mid (B_z \subseteq A)\} \tag{3}$$

Dilation is the opposite of erosion in mathematical morphology and it enlarges the boundaries of foreground regions. In a VBN chain, it is used to recover the original size of the body of interest after shrinking by erosion. Mathematically, dilation (defined in Equation 4) is represented by the $\oplus$ symbol and is defined as $A, \oplus, B$, where $\hat{B}$ is the reflection of B translated by a vector z over image A, evaluating whether the union with A is not an empty set.

$$A \oplus B = \{z | (\hat{B})_z \cap A \neq \emptyset\} \tag{4}$$

Connected Component Analysis (CCA) [Samet and Tamminen, 1988] is a technique based on identifying *blobs* in images. Blobs are areas on an image where pixels are connected and correspond to a unique category. After running a CCA algorithm over an image, a data structure containing a set of categories and a set of pixel pairs corresponding to each category is produced.

The CCA is organised into two passes. In the first pass, the image is iterated by columns (x direction) and then rows (y direction). For each pixel, first its location in the foreground (pixel value of 1) or in the background (pixel value of 0) is analysed. If it is in the foreground, then the neighbouring pixels. If no neighbours are also in the foreground, the pixel is assigned a label. If there are other neighbours in the foreground, the smallest label from the ones assigned to such neighbours is set to the inspected pixel. The rest of the labels, if they exist, are saved in an equivalence structure that links each label to other equivalent labels. In the second pass, the same iteration is performed. For each pixel, if it is in the foreground, it is relabelled by looking at the lowest equivalent label in the label equivalence structure.

3.4 Edge Detection algorithms

The techniques available in the Edge Detection block of the VBN Simulator are used to determine the contour of the body of interest for later execution of the Ellipse Fitting block. These algorithms take an image as an input and return a list of edge coordinates. Edge points are those in which gradient magnitude achieves a local maxima in the direction of the gradient.

Roberts, Prewitt, and Sobel operators

The Roberts, Prewitt, and Sobel operators are all edge detection methods based on convoluting an input image with filters approximating horizontal and vertical gradients. The Roberts operator, introduced in 1963 [Roberts, 1965] is the first and simplest one. In 1970, Prewitt presented a more complex discrete differentiation operator, made of two 3×3 filters instead of 2×2 ones. By having a "central" pixel in the kernels, the Prewitt operator can compute the gradient of the image *at* one position (corresponding to the image pixel underneath the central pixel of the filter as the latter is convoluted over the image) instead of the gradient of the image *between* two positions (which is what a 2×2 filter can yield).

Sobel presented in 1973 a very similar operator [Sobel and Feldman, 1973] which approximates horizontal and vertical derivatives with a 3×3 filters, but giving a bigger weight to central elements than lateral ones. The Prewitt operator presented before tends to lose detail of differences in specific rows or columns because of taking into account many neighbours with the same weight. This

is avoided by the Sobel operator, since it emphasises pixels closer to the centre of the filter. Table 1 depicts the discussed operators.

Table 1: Horizontal and vertical gradients filters for the Roberts, Prewitt, and Sobel operators.

	Roberts	***Prewitt***	***Sobel***
Horziontal gradient	$H_f = \begin{bmatrix} 1, & 0 \\ 0, & -1 \end{bmatrix}$	$H_f = \begin{bmatrix} 1, & 0, & -1 \\ 1, & 0, & -1 \\ 1, & 0, & -1 \end{bmatrix}$	$H_f = \begin{bmatrix} 1, & 0, & -1 \\ 2, & 0, & -2 \\ 1, & 0, & -1 \end{bmatrix}$
Vertical gradient	$V_f = \begin{bmatrix} 0, & 1 \\ -1, & 0 \end{bmatrix}$	$V_f = \begin{bmatrix} 1, & 1, & 1 \\ 0, & 0, & 0 \\ -1, & -1, & -1 \end{bmatrix}$	$V_f = \begin{bmatrix} 1, & 2, & 1 \\ 0, & 0, & 0 \\ -1, & -2, & -1 \end{bmatrix}$

For the Roberts, Prewitt, and Sobel operators, the filters (H_f, V_f) are convoluted with the input image I_{in}. The output image I_{out} is the square root of the convolutions' squares sum, as per Equation 5.

$$I_{out} = \sqrt{(H_f * I_{in})^2 + (V_f * I_{in})^2} \tag{5}$$

Laplacian of Gaussian operator

The Laplacian of Gaussian (LOG) [Kong et al., 2013] operator eliminates noise and uses a second-order operator to compute gradients, in contrast to the previously described first-order operators. It convolves the image with the Laplacian of a 2D Gaussian filter function. The LOG function is defined as per Equation 6, where σ is the standard deviation of the Gaussian noise, x and y are the coordinates of a point in the image, and e is the exponential function.

$$LoG(x, y) = -\frac{1}{\pi\sigma^4}\left[1 - \frac{x^2 + y^2}{2\sigma^2}\right]e^{-\frac{x^2+y^2}{2\sigma^2}} \tag{6}$$

The resulting image I_{out} is the result of convolving the input one I_{out} with the LoG function, as shown in Equation 7.

$$I_{out} = I_{in} * LoG \tag{7}$$

The LOG has however two main drawbacks, the first being that it sometimes produces false edges, and that it does not always work for very curved edges, but it remains a rather simple alternative with few computational/algorithmic steps.

Canny operator

In 1986, Canny presented a more complex method for detecting the edges of objects present on images [Canny, 1986]. Based on performing a series of sequential steps, it solves the problem of false edges shown by the LOG operator. In the first step of a Canny edge detector, the input image I is convolved with the Gaussian filter G generating the filtered image S, as Equation 8 represents.

$$S_{ij} = G_{ij} * I_{ij} \tag{8}$$

Then, in the second step, the 1st-order gradients of the image in the horizontal and vertical directions, P_{ij} and Q_{ij}, are computed approximately as Equation 9 and Equation 10 show, and as proposed in literature [Li et al., 2013].

$$P_{ij} \approx \frac{S_{i,j+1} - S_{ij} + S_{i+1,j+1} - S_{i+1,j}}{2} \tag{9}$$

$$Q_{ij} \approx \frac{S_{ij} - S_{i+1,j} + S_{i,j+1} - S_{i+1,j+1}}{2} \tag{10}$$

In the third step, the gradient magnitude matrix M is defined as per Equation 11, as the square root of the sum of the squares of the horizontal P_{ij} and vertical Q_{ij} image gradients.

$$M_{ij} = \sqrt{P_{ij}^2 + Q_{ij}^2} \tag{11}$$

Next, in the fourth step, it is checked whether a gradient magnitude is a local maximum in the direction of the gradient. For doing that, the Non-Maxima Suppression (NMS) method is used. If a pixel $[i, j]$ is a local maximum with respect to the adjacent pixels in the gradient direction, then its value is preserved, otherwise, M_{ij} is set to 0.

Finally, in the fifth step, a process called double threshold is performed. Two different thresholds τ_1 and τ_2, with τ_1 being a low value and τ_2 a high one, are defined. When setting a low threshold, noisy maxima will remain in the image. Whereas some true maxima might be discarded while setting a high value. Thus, the two thresholds are applied, and then the two thresholded images I_1 and I_2 are linked. The goal is to connect the gaps that are found in I_2 between edge points, that occur due to the high threshold that was used. When a gap is found in I_2, the corresponding edge is inspected in I_1, and connected neighbours are taken into account to close the gap in I_2. This produces the final image resulting from the Canny edge detector.

3.5 Ellipse Fitting algorithms

An ellipse $F(x, y)$ is a conic defined in its implicit equation form as Equation 12 shows, where A, B, C, D, E, and F are the ellipse parameters.

$$F(x, y) = Ax^2 + Bxy + Cy^2 + Dx + Ey + F = 0 \tag{12}$$

Among the myriad of different ways in which it can be expressed, the ellipse can also be described in its canonical equation form as Equation 13 shows, where $[x_0, y_0]$ represents the origin of the ellipse, a its semi-major axis, b its semi-minor axis, and α the angle of rotation about its origin.

$$\frac{((x - x_0)\ cos(\alpha) + (y - y_0)\ sin(\alpha))^2}{a^2} + \frac{((x - x_0)\ sin(\alpha) - (y - y_0)\ cos(\alpha))^2}{b^2} = 1 \tag{13}$$

At the end of the ellipse fitting process, the set of A, B, C, D, E, and F parameters, or rather the set of x_0, y_0, a, b, and α parameters (both sets that are inter-convertible) are to be obtained. Mathematically, fitting an ellipse onto a set of points that correspond to the contour or edge of the body of interest is an optimization problem in which the objective function to be minimised is the distance between the set of points and the ellipse.

Such minimization problem be formulated as per Equation 14, where J is the function to be optimized (in mathematical terms, the *cost function*), which is the sum of the squared distances d between the ellipse, represented by a vector of ellipse parameters $\vec{a} = [A\ B\ C\ D\ E\ F]$, and each of the points in a vector of edge candidate points $\vec{x_i}$.

$$min(J(\vec{a})) = min(\Sigma_{i=1}^{n}[d(\vec{a}, \vec{x_i})]^2) \tag{14}$$

Two types of distances d from the set of points to the ellipse can be used: the algebraic distance or the geometric distance. Using the algebraic distance allows for the direct resolution of the optimization problem with a least-squares approach, after the application of different normalisations or constraints to avoid getting the trivial solution $A = B = C = D = E = F = 0$. In this work, the normalisation $A + C = 1$, the normalisation $F = 1$, the constraint $4AC - B^2 = 1$, and an improved way of fitting with separately design and scatter matrices, proposed by [Halir and Flusser, 1998], are tested.

If applying the normalisations, solving the linear equation $A_m X_m = B_m$ retrieves the vector of implicit ellipse parameters X_m, with A_m and B_m defined as per Equation 16 for $A+C = 1$ normalisation and as per Equation 16 for $F = 1$ normalisation.

$$A_m = \begin{bmatrix} \Sigma_i(x_i^2 - y_i^2)^2, \Sigma_i(x_i^2 - y_i^2)x_i y_i, \Sigma_i(x_i^2 - y_i^2)x_i, \Sigma_i(x_i^2 - y_i^2)y_i, \Sigma_i(x_i^2 - y_i^2) \\ \Sigma_i(x_i^2 - y_i^2)x_i y_i, \Sigma_i(x_i^2 y_i^2), \Sigma_i(x_i^2 y_i), \Sigma_i(x_i y_i^2), \Sigma_i x_i y_i \\ \Sigma_i(x_i^2 - y_i^2)x_i, \Sigma_i x_i^2 y_i, \Sigma_i x_i^2, \Sigma_i x_i y_i, \Sigma_i x_i \\ \Sigma_i(x_i^2 - y_i^2)y_i, \Sigma_i x_i y_i^2, \Sigma_i x_i y_i, \Sigma_i y_i^2, \Sigma_i y_i \\ \Sigma_i(x_i^2 - y_i^2), \Sigma_i x_i y_i, \Sigma_i x, \Sigma_i y, \Sigma_i i \end{bmatrix} \quad B_m = -\begin{bmatrix} \Sigma_i(x_i^2 - y_i^2)y_i^2 \\ \Sigma_i x_i y_i^3 \\ \Sigma_i x_i y_i^2 \\ \Sigma_i y_i^3 \\ \Sigma_i y_i^2 \end{bmatrix} \tag{15}$$

$$A_m = \begin{bmatrix} \Sigma_i x_i^4, \Sigma_i x_i^3 y_i, \Sigma_i x_i^2 y_i^2, \Sigma_i x_i^3, \Sigma_i x_i^2 y_i \\ \Sigma_i x_i^3 y_i, \Sigma_i x_i^2 y_i^2, \Sigma_i x_i y_i^3, \Sigma_i x_i^2 y_i, \Sigma_i x_i y_i^2 \\ \Sigma_i x_i^2 y_i^2, \Sigma_i x_i y_i^3, \Sigma_i y_i^4, \Sigma_i x_i y_i^2, \Sigma_i y_i^3 \\ \Sigma_i x_i^3, \Sigma_i x_i^2 y_i, \Sigma_i x_i y_i^2, \Sigma_i x_i^2, \Sigma_i x_i y_i \\ \Sigma_i x_i^2 y_i, \Sigma_i x_i y_i^2, \Sigma_i y_i^3, \Sigma_i x_i y_i, \Sigma_i y_i^2 \end{bmatrix} \quad B_m = -\begin{bmatrix} \Sigma_i x_i^2 \\ \Sigma_i x_i y_i \\ \Sigma_i y_i^2 \\ \Sigma_i x_i \\ \Sigma_i y_i \end{bmatrix} \tag{16}$$

If applying the $4AC - B^2 = 1$ constraint, a design matrix D_m and a scatter matrix S_m can be defined, altogether with the constrain matrix C_m, as per Equation 17. Then, solving the eigensystem $S_m\vec{a} = \lambda C_m\vec{a}$ returns the vector of implicit ellipse parameters $\vec{a}$.

$$D_m = \begin{bmatrix} x^2 \\ xy \\ y^2 \\ x \\ y \\ 1 \end{bmatrix} \quad S_m = D_m' D_m \quad C_m = \begin{bmatrix} 0,0,-2,0,0,0 \\ 0,1,0,0,0,0 \\ -2,0,0,0,0,0 \\ 0,0,0,0,0,0 \\ 0,0,0,0,0,0 \\ 0,0,0,0,0,0 \end{bmatrix} \tag{17}$$

Finally, an improved, also direct fitting proposed by [Halir and Flusser, 1998] divides the design matrices and scatter matrices into quadratic and linear ones, proposes intermediary matrices T and M retrieves the ellipse implicit parameters vector X_m by using the solution a_1 to a proposed eigensystem, as summarised in Equation 18.

$$\begin{cases} D_1 = \begin{bmatrix} x^2 \\ xy \\ y^2 \end{bmatrix} \\ D_2 = \begin{bmatrix} x \\ y \\ 1 \end{bmatrix} \end{cases} \quad \begin{cases} S_1 = D_1' D1 \\ S_2 = D_1' D_2 \\ S_3 = D_2' D_2 \\ T = -S_3^{-1} S_2' \\ M = S_1 + S_2 T \end{cases} \quad Ma_1 = \lambda a_1 \quad X_m = \begin{bmatrix} a_1 \\ Ta_1 \end{bmatrix} \tag{18}$$

Using the geometric distance is advantageous since it avoids the *high curvature bias* that is found when fitting ellipses using algebraic distance. This problem arises when two edge candidate points that are at the same physical, geometric distance from the ellipse, shows two very different algebraic distances because one of the edge candidate points lies along the bigger semi-major axis a, and the other one lies along the smaller semi-minor axis b. Geometric distance does not exhibit this bias. The disadvantage of using this distance is that no direct resolutions are possible, having to use iterative numerical methods, thus more computationally intensive and not always deterministic. Additionally, a first guess of the ellipse is needed in order to be run.

Thus, using a method based on algebraic distance is required first, and this initial guess is then refined by the methods using geometric distance. In particular, two numerical methods are tested in this work: the Gauss-Newton, as per [Ahn et al., 1999], and the Levenberg-Marquadt, as per

[Barham and Drane, 1972]. In this work, the initial guess of the ellipse fed to the numerical methods is produced by the improved direct ellipse fitting techniques presented before.

Additionally, this work has explored robust methods, which aim to separate useful points (known as inliers) from noise points (known as outliers), fitting an ellipse with a smaller but cleaner set of edge candidates, and ultimately obtaining a more accurate fitted ellipse. Two methods of the family of Sample Consensus methods, the Random Sample Consensus (RANSAC) [Fischler and Bolles, 1981] and the M-Estimator Sample Consensus (MSAC) [Torr and Zisserman, 2000] are tested in this work.

With these methods, a subset of edge candidate points is first randomly selected. This subset is then used to estimate the ellipse parameters using one of the previously described methods based either on the algebraic or on the geometric distance. In this case, the initial guess is also produced by the improved direct ellipse fitting techniques. Next comes the phase of evaluating the fitted ellipse. The distance of the fitted ellipse to the rest of the edge points (those initially considered *outliers*) is computed. If the distance is below a given threshold for an edge point, this point is added to the list of *inliers*. Then, the loss of the fitted ellipse is computed with respect to all the *inlier* points, the ones that were selected randomly first, and the ones that were added later. This loss function is defined by Equation 19 (on the left, the loss for the RANSAC; on the right, for the MSAC), where ρ is the loss function, which depends on the distance d from the i-th edge point $\vec{x}_i$ to a fitted ellipse with a vector of parameters $\vec{p}$. t is a threshold set to compute the error. The fit of the ellipse producing the lower loss is the one kept at the end of the process.

$$\rho(\vec{x}_i, \vec{p}) = \begin{cases} 0 \textbf{ if } |d(\vec{x}_i, \vec{p})| < t \\ k \textbf{ if } |d(\vec{x}_i, \vec{p})| \geq t \end{cases} \qquad \rho(\vec{x}_i, \vec{p}) = \begin{cases} d(\vec{x}_i, \vec{p})^2 \textbf{ if } d(\vec{x}_i, \vec{p})^2 < t^2 \\ t^2 \qquad\qquad \textbf{if } d(\vec{x}_i, \vec{p})^2 \geq t^2 \end{cases} \tag{19}$$

3.6 LOS calculation

Once an ellipse has been fitted to the body to be navigated, the centroid of this body can be approximated to the centre of the ellipse. Given the ellipse's implicit equation parameters A, B, C, D, E, F, its centre coordinates $[x_0, y_0]$ are calculated as shown in Equation 20 and 21.

$$x_0 = \frac{2CD - BE}{B^2 - 4AC} \tag{20}$$

$$y_0 = \frac{2AE - BD}{B^2 - 4AC} \tag{21}$$

These coordinates are the $[u_i, v_i]$ in Equation 2, which allows to compute the LOS vector.

3.7 Simulations

The simulation scenario is the environment in which a given combination of VBN algorithms is executed. It includes the description of the body of interest to navigate (in this case, an asteroid), the spacecraft that is taken into account and its associated camera(s), and the trajectory points that

are used used for image generation. Table 2 presents a summary of the items and values of the global simulation scenario, which are explained in detail in the following subsections.

Table 2: Summary of the global simulation scenario.

Scenario item	Value
Asteroid	(25143) Itokawa
Spacecraft	Juventas
Visible camera	OCAMS SamCam (OSIRIS-REx)
Infrared camera	TIR (Hayabusa 2)
Orbits	INSP phase, 23000 m distance SSTO phase, 3300 m distance
Asteroid poses	Centred, rotated 5° or 2.5° to the left, right, top & bottom

In order to reduce the number of combinations to be tested, a *golden standard* is defined both for the Edge Detection and for the Ellipse Fitting block. For each block, all the possible algorithms are tested, using the corresponding golden standard for the other block. Additionally, a simulation using the COB centroid estimation method is performed as a benchmark and to confirm the improvement of the new Ellipse Fitting methods.

For the Edge Detection block, the **Canny edge detector** is set the golden standard. Among the implemented algorithms, it is the most complete, albeit more computationally intensive. For the Ellipse Fitting block, the **improved direct least-squares ellipse fitting** based method on the algebraic distance is chosen as the golden standard. It is the most sophisticated of the implemented algebraic-distance-based algorithms, which do not require iterations to reach convergence and are thus deterministic, giving it an edge over geometric-distance-based and resilient approaches.

For the geometric-distance-based methods, the following parameters, related to the numerical methods, are used during the presented simulations: the simulation step is 0.025 for a total number of 30 iterations, in the case of the Levenberg-Marquadt numerical method, the Lambda correcting parameter is set to $\lambda = 1$. In the case of robust methods, these are the parameters used in the mentioned simulations: the number of initial randomly selected inliers is 45, the maximum number of iterations is 2000, the error threshold is set to 5×10^{10} and the minimum required number of inliers is 120.

In order to reduce the number of combinations to be tested, a *golden standard* is defined both for the Edge Detection and for the Ellipse Fitting block. For each block, all the possible algorithms are tested, using the corresponding golden standard for the other block. Additionally, a simulation using the COB centroid estimation method is performed as a benchmark and to confirm the

improvement of the new Ellipse Fitting methods.

- **Distance:** 3300 m.
- **Image type:** VIS images (10 images).
- **Image Processing block:** Brightening factor of 7, binarisation and rotation applied, erosion size $[5, 5]$ px, dilation size $[10, 10]$ px. On a first simulation case, no CCA is used. On a second one, CCA is activated.
- **Edge Detection block:** Canny edge detector.
- **Ellipse Fitting block:** Algebraic-distance-based improved direct least-squares.
- **Simulations per image:** $n = 10$.
- **Standard dev. of Gaussian noise:** $\sigma = 0.125$.

Additionally, a simulation using the COB is performed to compare the results between the two types of centroid estimation when a noisy image is used.

Already during the validation of the VBN Simulation, it was seen that the presence of big areas of shadow on the surface of the asteroid degrade the performance of the VBN chain. Because of that, it was decided to implement a novel correction block adding three correction possibilities: the use of an *a-priori* asteroid shape model, the implementation of a star eclipse method, and the utilisation of thermal images.

Since the need for image correction due to shadowing is only experienced in visible-spectrum images at close distances to the asteroid, only VIS images at 3300 m (10 images) are used. Again, the gold standard is used. The parameters used for the corrected simulations are described below:

- **Distance:** 3300 m.
- **Image type:** VIS images (10 images).
- **Image Processing block:** Brightening factor of 7, binarisation and rotation applied, no CCA, erosion size $[5, 5]$ px, dilation size $[10, 10]$ px.
- **Edge Detection block:** Canny edge detector.
- **Ellipse Fitting block:** Algebraic-distance-based improved direct least-squares.

4. Results

This section goes over the results obtained when performing the simulations outlined before, aiming to understand whether ellipse fitting methods are better than the COB method, and which of the ellipse fitting algorithmic combinations work best for each scenario.

4.1 Nominal simulation results

Nominal simulations are divided into two blocks of combinations, in which all implemented algorithms are used, tested together with the gold standard algorithm of the other VBN block. First, Edge Detection combinations are tested and compared (with the least-squares-based algebraic distance improved fitting as the gold standard in the Ellipse Fitting block), later Ellipse Fitting combinations are tested and compared (with the Canny edge detector as the gold standard in the Edge Detection block). Numerical results are depicted in Table 3 for Edge Detection and in Table 4 for Ellipse Fitting.

Table 3: Results of the nominal simulations with the different Edge Detection algorithms (coupled with the least-squares-based algebraic distance improved ellipse fitting), for 3300 m and 23000 m. Centre of Brightness results provided for comparison on the first row. Mean simulation time on MATLAB, mean absolute centroid error (distance simulated centroid and reference), mean absolute LOS vector error (angle between simulated vector and reference), and mean relative centroid and mean LOS vector errors are provided, together with the standard deviation.

	Sim. time [ms]	**Abs. centr. err. (dist. sim.-ref.) [px]**	**Abs. LOS err. (angle sim.-ref.) [°]**	**Rel. centr. error [%]**	**Rel. LOS error [%]**
	3300 m				
COB	56.80 ± 5.04	180.87 ± 156.22	3.35 ± 3.00	11.34 ± 10.33	5.85 ± 5.23
Roberts	31.10 ± 1.99	76.31 ± 35.56	1.74 ± 0.70	4.35 ± 1.84	3.03 ± 1.22
Prewitt	26.87 ± 5.07	76.34 ± 35.68	1.74 ± 0.70	4.36 ± 1.88	3.04 ± 1.22
Sobel	25.06 ± 2.16	75.95 ± 35.57	1.73 ± 0.70	4.34 ± 1.86	3.03 ± 1.22
LOG	241.39 ± 8.04	75.24 ± 35.17	1.72 ± 0.69	4.29 ± 1.83	3.00 ± 1.21
Canny	46.96 ± 2.69	76.56 ± 35.87	1.75 ± 0.70	4.38 ± 1.88	3.05 ± 1.23
	23000 m				
COB	56.85 ± 3.28	18.17 ± 11.38	0.70 ± 0.51	1.12 ± 0.64	1.23 ± 0.89
Roberts	28.98 ± 2.89	13.00 ± 5.37	0.66 ± 0.52	0.73 ± 0.32	1.15 ± 0.92
Prewitt	22.99 ± 1.42	13.00 ± 5.77	0.66 ± 0.53	0.74 ± 0.36	1.16 ± 0.93
Sobel	25.56 ± 2.17	12.88 ± 5.67	0.66 ± 0.53	0.74 ± 0.36	1.15 ± 0.93
LOG	247.28 ± 16.44	12.69 ± 5.52	0.66 ± 0.53	0.72 ± 0.34	1.15 ± 0.93
Canny	44.51 ± 2.17	12.90 ± 5.55	0.66 ± 0.53	0.73 ± 0.34	1.15 ± 0.93

Table 4: Results of the nominal simulations with the different Ellipse Fitting algorithms coupled with the Canny edge detector, for 3300 m and 23000 m. Centre of Brightness results provided for comparison on the first row. Mean simulation time on MATLAB, mean absolute centroid error (distance simulated centroid and reference), mean absolute LOS vector error (angle between simulated vector and reference), and mean relative centroid and mean LOS vector errors are provided, together with the standard deviation. Legend: AD: Algebraic Distance / N: Normalisation / CON: Constraint / IMP: Improved direct fit / GD: Geometric Distance / GN: Gauss-Newton / LM: Levenberg-Marquadt.

	Sim. time [ms]	**Abs. centr. err. (dist. sim.-ref.) [px]**	**Abs. LOS err. (angle sim.-ref.) [°]**	**Rel. centr. error [%]**	**Rel. LOS error [%]**
	3300 m				
COB	56.80 ± 5.04	180.87 ± 156.22	3.35 ± 3.00	11.34 ± 10.33	5.85 ± 5.23
AD N1	61.56 ± 7.13	190.40 ± 322.82	3.77 ± 5.86	12.16 ± 22.22	6.55 ± 10.17
AD N2	74.75 ± 18.46	199.88 ± 285.32	4.02 ± 5.08	12.40 ± 18.57	7.01 ± 8.84
AD CON	60.91 ± 7.35	76.56 ± 35.87	1.75 ± 0.70	4.38 ± 1.88	3.05 ± 1.23
AD IMP	60.28 ± 6.83	76.56 ± 35.87	1.75 ± 0.70	4.38 ± 1.88	3.05 ± 1.23
GD GN	2573.16 ± 528.96	96.36 ± 44.85	2.06 ± 0.84	5.61 ± 2.57	3.59 ± 1.47
GD LM	3185.42 ± 886.66	74.02 ± 39.38	1.69 ± 0.76	4.32 ± 2.18	2.96 ± 1.33
RANSAC	534.36 ± 124.73	77.41 ± 36.89	1.75 ± 0.75	4.56 ± 2.00	3.05 ± 1.31
MSAC	437.56 ± 23.64	73.60 ± 41.05	1.71 ± 0.83	4.20 ± 2.28	2.98 ± 1.44
	23000 m				
COB	56.85 ± 3.28	18.17 ± 11.38	0.70 ± 0.51	1.12 ± 0.64	1.23 ± 0.89
AD N1	67.19 ± 13.49	13.44 ± 6.38	0.67 ± 0.52	0.76 ± 0.41	1.16 ± 0.91
AD N2	51.82 ± 6.47	12.99 ± 5.46	0.65 ± 0.52	0.75 ± 0.34	1.14 ± 0.90
AD CON	56.94 ± 13.25	12.90 ± 5.55	0.66 ± 0.53	0.73 ± 0.34	1.15 ± 0.93
AD IMP	44.51 ± 2.17	12.90 ± 5.55	0.66 ± 0.53	0.73 ± 0.34	1.15 ± 0.93
GD GN	364.17 ± 118.34	16.45 ± 7.49	0.71 ± 0.56	0.95 ± 0.48	1.24 ± 0.99
GD LM	649.90 ± 191.90	12.81 ± 5.39	0.66 ± 0.53	0.73 ± 0.33	1.15 ± 0.93
RANSAC	455.41 ± 32.29	12.77 ± 5.65	0.66 ± 0.54	0.74 ± 0.36	1.15 ± 0.94
MSAC	446.14 ± 27.66	13.94 ± 6.10	0.68 ± 0.54	0.79 ± 0.38	1.19 ± 0.94

A global conclusion can be extracted, however, since it is common for all the performed simulations: the centroid determination via ellipse fitting, in all of its possible algorithmic combinations, performs better than the centroid determination via COB determination. The computational effort

in terms of simulation time is on the same order of magnitude, however, **accuracy improvements range from 0.5 to 7 percent points for the relative centroid error, and up to 2.8 percent points for the relative LOS error**.

4.2 Degraded simulation results

When running the degraded simulations, using the COB method; and with and without the CCA activated, when using the ellipse fitting gold standard, it can be seen (as per Table 5) that the inclusion of white Gaussian noise effectively hampers the performance of the VBN chain, degrading the results, which are **5 percent points higher without CCA**. However, the usage of the CCA algorithm allows to have results much more similar to the ones obtained when simulating non-perturbed images (only 0.5 percent points higher). This shows that even for remarkable signal noise, the usage of the proper algorithms such as CCA allows to obtain acceptable results. Thus, very degraded image sensor conditions will not completely preclude the usage of VBN. However, since simulation time also increases in two orders of magnitude, care must be taken to use these methods as a last resource when they are essential.

Table 5: Degraded simulations' results with the gold standard, 10 images at 3300 m, without and using CCA. Centre of Brightness results also shown for reference. Mean simulation time on MATLAB, mean absolute centroid error (distance simulated centroid and reference), mean absolute LOS vector error (angle between simulated vector and reference), and mean relative centroid and mean LOS vector errors are provided, together with the standard deviation.

	Sim. time [s]	**Abs. centr. err. (dist. sim.-ref.) [px]**	**Abs. LOS err. (angle sim.-ref.) [°]**	**Rel. centr. error [%]**	**Rel. LOS error [%]**
COB	0.59 ± 0.09	208.02 ± 137.76	71.63 ± 0.09	13.39 ± 9.12	6.73 ± 4.67
GS, no CCA	3.72 ± 2.07	240.48 ± 95.11	71.64 ± 0.04	13.35 ± 5.15	8.36 ± 3.40
GS, CCA	226.88 ± 135.21	91.02 ± 45.14	71.58 ± 0.01	5.19 ± 2.48	3.57 ± 1.44

However, it can be seen that using the centroid determination via the COB method can also be beneficial in situations of high noise. Indeed, for an additive and randomly spread noise on the image, the centre of brightness of the image is not expected to change if the noise is not extremely high. Although ellipse fitting methods outperform the COB one in high noise situations if the CCA is active (improvements of 8 percent points in relative centroid error and of 3 percent points in relative LOS error), computing time is also several orders of magnitude higher, and thus, the currently used COB method may remain a better option in flight.

4.3 Corrected simulation results

The recent integration of a piece of code furnished to us by the *AOCS Architecture* service from the CNES, which enables both the generation of a sky window -given an attitude- without the asteroid present, and the correlation of the stars present in such sky window with the ones present on the simulated asteroid image (finally determining which stars have been shadowed by the asteroid), has enabled running the first tests and simulations of the correction method using eclipsed stars.

The results for this correction method, particularly promising, are shown graphically in Figure 5 and 6, where two different asteroid images in which the level of shadowing is important are simulated. On the pictures on the left, the output from the Ellipse Fitting block shows how the large areas of shadows impede the VBN chain to properly fit an ellipse around the asteroid's real contour. Pictures on the right shows the result once the Correction block is activated and the star eclipse correction method is applied: eclipsed stars are detected (encircled in green) and are used to successfully extend the initially filled ellipse in order to cover the whole asteroid.

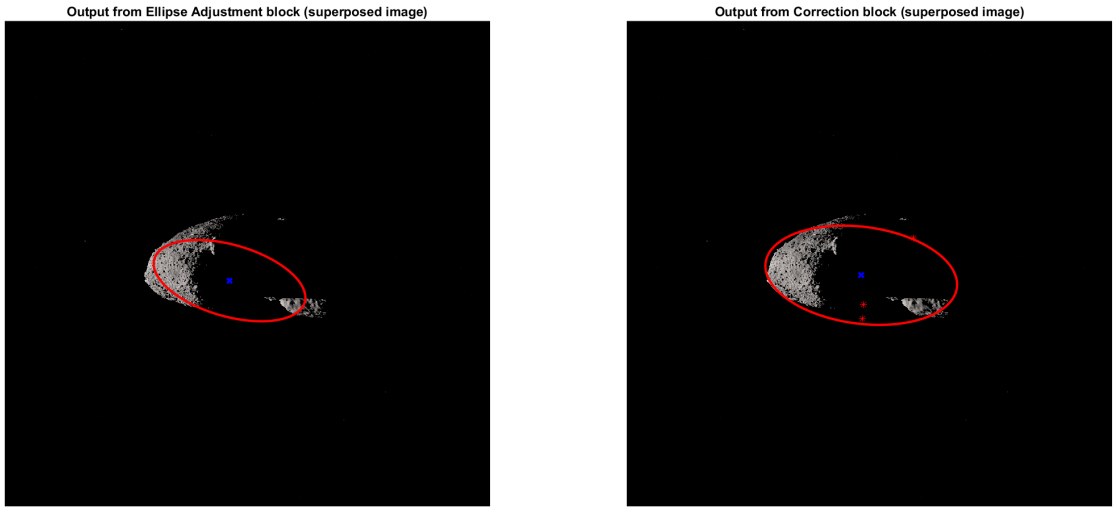

(a) Output from the Ellipse Fitting block.

(b) New output after the Correction block.

Figure 5: Simulated image after exiting the Ellipse Fitting block without a correction, and after exiting the Correction block (image 1/2).

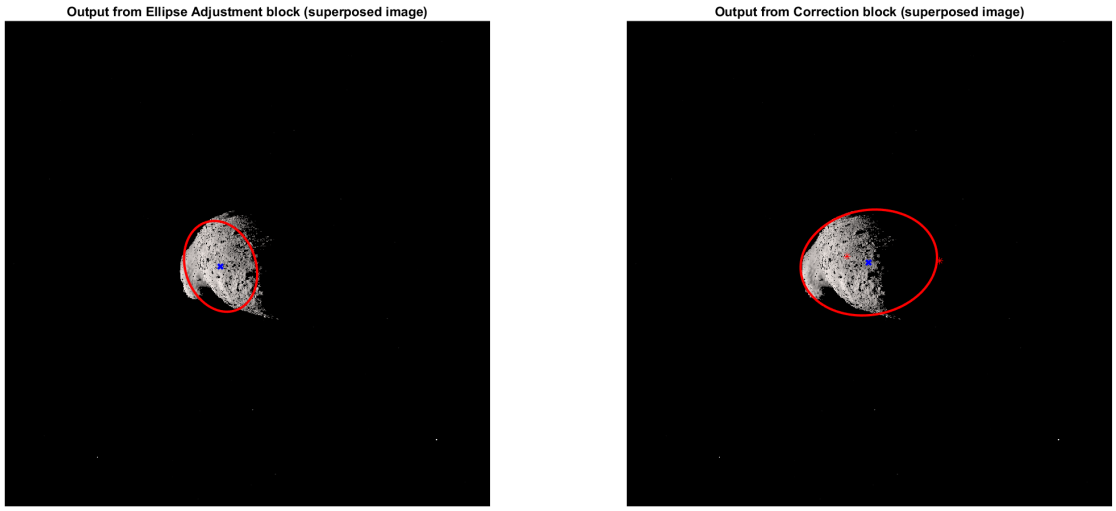

(a) Output from the Ellipse Fitting block.

(b) New output after the Correction block.

Figure 6: Simulated image after exiting the Ellipse Fitting block without a correction, and after exiting the Correction block (image 2/2).

The introduction of the correction method **reduces the relative centroid error by around 2.4 percent points**, and **reduces the relative LOS error by about 1.4 percent points**.

5. Discussion

The presentation of the material and methods, theory and calculations, and results allow us to perform a series of considerations on relevant topics related to the work.

Relevance of VBN

The role of Vision Based Navigation (VBN) in interplanetary missions was studied. It was found that VBN has been crucial for close relative navigation and landing on small bodies such as asteroids, comets and other small bodies, due to the delay in Earth-spacecraft communications. The most widely used techniques for VBN are centroiding via the determination of the Centre of Brightness (COB) for close operations and landmark tracking for landing.

Techniques' improvement

A state-of-the-art study was performed on Vision Based Navigation (VBN) techniques, focusing on the improvement of accuracy and performance of currently studied techniques compared to those used in flight. It was found that VBN for space operations is a widely researched topic, and many different proposals are being explored to enhance current techniques such as centroiding via COB determination. New techniques, such as centroiding via ellipse fitting, and the usage of Deep Learning (DL) methods are being explored. However, current hardware limitations do not allow for the usage of more computationally-intensive methods, and questions on the possibility of em-

barking DL techniques remain. Therefore, this work focused on studying ellipse fitting methods and through simulation, it was found that these methods perform better than the centroiding via COB currently in use in interplanetary missions, producing more accurate results with equivalent computational effort.

Algorithm comparison

A modular framework called the VBN Simulator was built to implement and simulate algorithms for different VBN chain blocks. The framework was successfully validated and different simulation cases were run. Results showed that algorithm performance is proportional to the distance between the asteroid and spacecraft, and that accuracy differences between Edge Detection algorithms are minor. The Laplacian of Gaussian operator was found to be the most accurate, but the Sobel operator is recommended for non-perturbed scenarios because of its faster computation time. For Ellipse Fitting algorithms, accuracy differences were more sensitive to the simulation environment, and different algorithms are recommended for different scenarios. The direct algebraic-distance-based least-squares improved fit is recommended for small apparent body sizes, while the M-Estimator Sample Consensus is recommended for big apparent body sizes. It was also observed that the initially thought "gold standard" combination of algorithms was not always the best. Different simulation cases advised the usage of different algorithm combinations.

Noisy and real environments

Since the asteroid images that were used to perform simulations and compare the VBN techniques were generated computationally and are not real (this is convenient to generate at the same time data references used to compute the simulation error), degraded simulations in which additive white Gaussian noise was added were performed. Additionally, real images from the DART mission were also used for simulation, albeit with no data references and thus no error computed at the end of such simulation.

Both degraded and real simulations showed the capacity of a well-equipped Image Processing block of rejecting most of the perturbing elements in simulations (high noise or presence of other bodies in the image). In this sense, the Connected Component Analysis (CCA) algorithm proved to be cornerstone in ensuring accuracy in such impairing situations, by focusing only on the body of interest to be navigated.

Surface shadowing

One of the intrinsic characteristics of many small bodies, particularly asteroids, is their irregularity, since it is linked to some common formation processes (e.g. aggregation of smaller bodies or progressive accumulation of rocks and dust). This irregularity, coupled with particular sunlight incidence angles, generates larges areas of shadow on the surface of the body.

Already since the validation of the VBN Simulator, it was seen that large shadowed regions greatly degrade the performance of the VBN techniques. With regards to the ones implemented in this work, the shadows particularly affect the Edge Detection block, since they hinder the proper identi-

fication of all the body contour points. In order to counteract the effect of shadowing, three different correction techniques were designed: the usage of *a priori* shape models, the usage of background stars eclipsed by the body, and the usage of thermal images. The last two have shown to provide good results, with a significant decrease of the error committed in simulations. In particular, the eclipsed stars method is more promising as it does not require new uncommon hardware such as IR navigation cameras, being able to be implemented with current navigation cameras and star trackers.

6. Conclusion

This work dived into Vision-Based Navigation techniques, a field which is still under development and which will surely power more autonomous, quicker, and safer operations in space. A profound study of the flight heritage and of the state of the art of was performed, and a series of algorithms were picked considering its mid-term deployment potential and promising performance. In particular, algorithms from the family of centroid determination via ellipse fitting were selected, being a natural evolution from the nowadays used centre of brightness used to determine a body's centroid. The different algorithms falling into this family were studied thoroughly, allowing for a mathematical approach to the intersection of image processing and navigation. The coding of a modular simulator allowing then to formally test and compare the algorithms and their different combinations was essential.

All in all, this work produced relevant simulation results, from which clear conclusions on the most interesting algorithmic combinations were drawn for different possible cases, and it proposed corrections not tackled currently in literature to solve some of the pitfalls of the studied techniques, such as the degradation of results in cases of large areas of shadows on the surface of navigated bodies.

Acknowledgements
The authors would like to acknowledge Sébastien Goulet for his contribution with Aurora, a software tool used to generate synthetic images of asteroids; as well as to Étienne Perot and Frédérick Viaud, for their code used to generate images of a window of sky with a given attitude.

References

[Ahn et al., 1999] Ahn, S. J., Rauh, W., and Recknagel, M. (1999). Ellipse fitting and parameter assessment of circular object targets for robot vision. In *Proceedings 1999 IEEE/RSJ International Conference on Intelligent Robots and Systems. Human and Environment Friendly Robots with High Intelligence and Emotional Quotients (Cat. No.99CH36289)*, volume 1, pages 525–530 vol.1.

[Barham and Drane, 1972] Barham, R. H. and Drane, W. (1972). An Algorithm for Least Squares Estimation of Nonlinear Parameters When Some of the Parameters Are Linear. *Technometrics*, 14(3):757–766.

[Canny, 1986] Canny, J. (1986). A Computational Approach to Edge Detection. *IEEE Transactions on Pattern Analysis and Machine Intelligence*, PAMI-8(6):679–698.

[Christian and Lightsey, 2010] Christian, J. and Lightsey, E. G. (2010). An On-Board Image Processing Algorithm for a Spacecraft Optical Navigation Sensor System. *AIAA SPACE 2010 Conference & Exposition*.

[Fischler and Bolles, 1981] Fischler, M. A. and Bolles, R. C. (1981). Random Sample Consensus: A Paradigm for Model Fitting with Applications to Image Analysis and Automated Cartography. *Commun. ACM*, 24(6):381–395.

[Halir and Flusser, 1998] Halir, R. and Flusser, J. (1998). Numerically Stable Direct Least Squares Fitting Of Ellipses.

[Kong et al., 2013] Kong, H., Akakin, H. C., and Sarma, S. E. (2013). A Generalized Laplacian of Gaussian Filter for Blob Detection and Its Applications. *IEEE Transactions on Cybernetics*, 43(6):1719–1733.

[Li et al., 2013] Li, S., Lu, R., Zhang, L., and Peng, Y. (2013). Image Processing Algorithms For Deep-Space Autonomous Optical Navigation. *Journal of Navigation*, 66(4):605–623.

[Okada, 2020] Okada, T. (2020). Thermography of Asteroid and Future Applications in Space Missions. *Applied Sciences*, 10(6).

[Prewitt, 1970] Prewitt, J. M. S. (1970). Object enhancement and extraction. *Picture Processing and Psychopictorics*, pages 75–149.

[Roberts, 1965] Roberts, L. G. (1965). Machine Perception of Three-Dimensional Solids. *Optical and Electro-Optical Information Processing*.

[Samet and Tamminen, 1988] Samet, H. and Tamminen, M. (1988). Efficient component labeling of images of arbitrary dimension represented by linear bintrees. *IEEE Transactions on Pattern Analysis and Machine Intelligence*, 10(4):579–586.

[Sobel and Feldman, 1973] Sobel, J. I. and Feldman, G. (1973). A 3x3 Isotropic Gradient Operator for Image Processing. *Pattern Classification and Scene Analysis*, pages 271–272.

[Torr and Zisserman, 2000] Torr, P. and Zisserman, A. (2000). MLESAC: A New Robust Estimator with Application to Estimating Image Geometry. *Computer Vision and Image Understanding*, 78(1):138–156.